2836 Vol. 46, No. 12 / 15 June 2021 / Optics Letters Letter

Check for updates

Optics Letters

C and L band room-temperature continuous-wave InP-based microdisk lasers grown on silicon

LIYING LIN, YING XUE, JIE LI, WEI LUO, JIE HUANG, AND KEI MAY LAU*

Department of Electronic and Computer Engineering, Hong Kong University of Science and Technology, Clear Water Bay, Kowloon, Hong Kong, China
*Corresponding author: eekmlau@ust.hk

Received 20 January 2021; revised 27 April 2021; accepted 17 May 2021; posted 17 May 2021 (Doc. ID 420106); published 7 June 2021

Quantum-dot (QD) and quantum-dash (QDash) have been shown to be promising gain materials for lasers directly grown on Si due to their better tolerance to crystal defects and thermal stability. Here we report optically pumped InP-based InAs QDash microdisk lasers (MDLs) directly grown on on-axis (001) Si. To the best of our knowledge, this is the first demonstration of room-temperature continuous-wave lasing of a QDash MDL on Si in the C band and L band. To the best of our knowledge, the lowest threshold of around 400 μW and highest operation temperature of 323 K have been achieved. An analysis of experimental results shows that the dominant lasing wavelength of MDLs varies with the thickness and diameter of the MDLs. Our demonstration shows potential application of MDLs for multi-channel operation in densely integrated Si-photonics. © 2021 Optical Society of America

https://doi.org/10.1364/OL.420106

Low-cost photonic integrated circuits on a Si platform compatible with the well-established complementary metal-oxide-semiconductor technology have been investigated for decades [1,2]. Despite the success of the group-IV-based optical building blocks, an efficient laser source is still the crux for fully integrated silicon photonics [3]. III-V-based heterogeneous Si lasers realized by die/wafer bonding present excellent performance [4]. Nevertheless, issues regarding the size and cost of III-V wafers, as well as the bonding yield, have yet to be fully resolved [4,5]. Direct growth of III-V materials on Si offers a promising alternative for low-cost and scalable integration. The main roadblock of direct hetero-epitaxial growth is the high density of defects induced by lattice, thermal, and polarity mismatches between III-V compounds and Si. While selective hetero-epitaxy produces dislocation-free III-V compounds on Si, the dimension of the epitaxial crystals is often limited, and the realization of electrically driven devices has been challenging [6,7]. In contrast, blanket hetero-epitaxy deposits large-dimension III-V thin films on Si wafers and engenders III-V/Si templates with low defect densities [8]. With quantum-dot (QD) and quantum-dash (QDash) as gain material, which show reduced sensitivity to threading dislocations, the impact of defects has been further mitigated [9,10]. InAs QD lasers monolithically grown on Si have been extensively researched in the past decade as telecom-band light sources [4,11–14].

A whispering-galley mode (WGM) microdisk laser (MDL) is considered as an attractive light source for dense integration due to the miniaturized volume and ultra-low power consumption [15]. The first room-temperature (RT) continuous-wave (CW) O band MDLs grown on Si was achieved in 2016 [16]. For the C band, however, only pulsed lasing and low-temperature CW lasing were reported [17–20]. In this Letter, we successfully demonstrate RT CW single-mode lasing from the QDash MDL on Si with a low threshold. The lasing characteristics of the MDLs enable us to carry out further investigation on the lasing wavelength as a function of physical parameters.

Figure 1(a) delineates the structure of epitaxial InAs QDash lasers on Si substrates. The epitaxial structures were grown in metalorganic chemical vapor deposition systems. To release the stress caused by the large lattice mismatch between InP and Si (8%), 1.1 μm GaAs was first grown on unpatterned planar Si as an intermediate buffer, followed by five cycles of thermal cycle annealing for further defect reduction. Then 3.1 μm InP with three sets of 10-period $In_{0.63}Ga_{0.37}As$ (12 nm)/InP (34 nm) strained layer superlattices were grown. The as-grown InP buffer is APB-free with a surface roughness of 2.8 nm measured by a surface atomic force microscope. Detailed information of growth was reported in a previous publication [21]. A three-layer InAs/InGaAs dash-in-well structure sandwiched by InAlAs cladding layers was then grown on the InP on Si (IoS) template. An identical MDL structure was also grown on InP native substrate in the same run for fair comparison. RT photoluminescence (PL) spectra of as-grown three layers of QDashes on Si and native InP substrate are shown in Fig. 1(b). All the peaks center on 1.5 μm, and the intensity of the one grown on InP is around three times higher than that grown on Si.

The fabrication process was reported in our previous works [16,22]. Considering that the WGMs concentrate on the

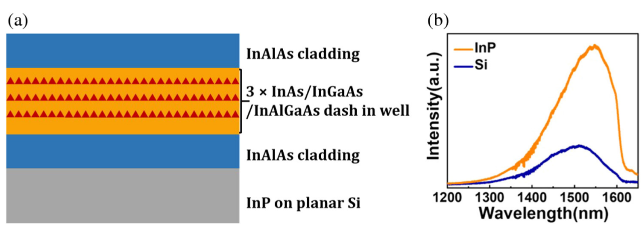

Fig. 1. (a) Structure schematic of the as-grown MDL on Si. (b) RT PL of the as-grown samples on InP and Si substrates.

0146-9592/21/122836-04 Journal © 2021 Optical Society of America

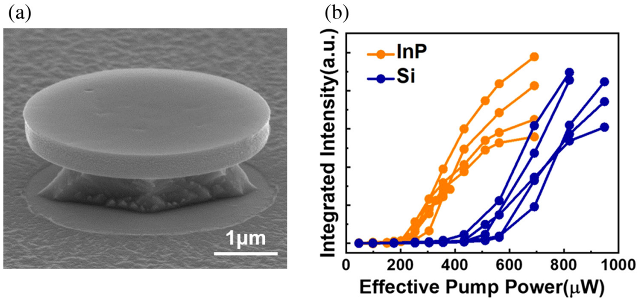

Fig. 2. (a) 70° tilted SEM image of a 4 μm diameter as-fabricated MDL on Si. (b) L-L curves of MDLs on InP and Si substrates. The kinks indicate the onset of the lasing operation. The thresholds of MDLs on native InP substrate concentrate at 200 μW, and the thresholds of MDLs on Si are around 500 μW.

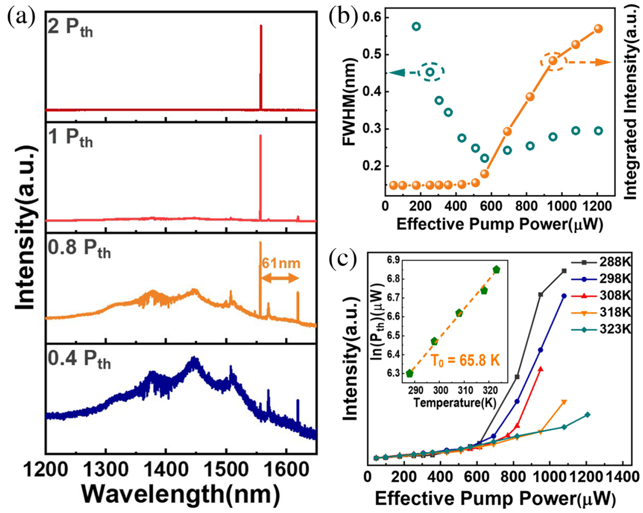

Fig. 3. (a) Representative power-dependent spectra of MDLs. (b) RT L-L curve and transition curve of the FWHM. (c) L-L curves at different temperatures ranging from 288 to 323 K. Inset: natural logarithm of threshold power against temperature. Characteristic temperature $T_0 = 65.8$ K in the range of 288–323 K.

periphery of MDLs, we focused on two aspects: a smooth sidewall for the low-loss WGMs resonance and a tight air cladding structure for good optical confinement [23]. In the fabrication process, a 900 nm high InP pedestal was formed with an undercut around 500 nm to prevent first-radial mode leakage into the underlying template and suppress high-radial order modes. The 70° tilted scanning electron microscope (SEM) image of the fabricated MDL is shown in Fig. 2(a). The thickness of the MDL structure is measured to be around 435 nm, and the diameter is 3.8 ± 0.3 μm.

Fabricated MDLs were characterized in a micro-PL system, with a 1064 nm CW laser as the excitation source. Considering multiple absorptions/reflections at the surface of MDLs [24,25], around 62% of pumping power was effectively absorbed. The extracted light-out/light-in (L-L) curves of MDLs on Si and InP substrates are summarized in Fig. 2(b). The thresholds were extrapolated to be around 200 and 500 μW for lasers on native InP substrate and on Si substrate, respectively. The larger thresholds of MDLs on Si correspond to the lower PL intensity of the as-grown sample on Si compared with InP substrate. RT power-dependent micro-PL spectra of the MDL on Si is shown in Fig. 3(a). Below the threshold, multiple modes were excited. With increasing pump power, one peak located at 1555 nm stood out and finally lased. Based on the structure of a specific MDL and effective indices of InAlAs and InAlGaAs obtained from experimental data in [26], we numerically calculated transverse electric (TE)- and transverse magnetic (TM)-polarized modes using the finite-difference time-domain (FDTD) method. The $TE_{19,1}$ mode (radial mode number $l = 1$, azimuthal mode number $m = 19$) has a resonant wavelength at 1559 nm, which matches the measured lasing wavelength. The L-L curve and transition curve of the full width at half-maximum (FWHM) extracted by bi-Lorentzian fitting can be seen in Fig. 3(b). The transition from spontaneous emission to lasing was evident by the narrowing of the FWHM down to around 0.25 nm after lasing. The high cold quality factor (Q) of the MDL can be calculated to be $\lambda/\Delta\lambda = 6220$ at pump power $\sim 0.9\ P_{\rm th}$, where λ represents the emission wavelength, and $\Delta\lambda$ is the FWHM of the lasing peak. This value is higher compared to the 1.55 μm band MDLs reported in the literature [15,18,19,27,28], which attests to the good circularity and smooth sidewall of fabricated microdisks. The small cavity of the MDL leads to a large free spectral range (FSR). As shown in Fig. 3(a), the mode spacing between the lasing mode and its adjacent mode in the same radial order are around 61 nm, which are in good agreement with the theoretical value of 62 nm derived from $\lambda^2/2\pi R n_g$, where n_g is the group index of the cavity, and R is the disk radius.

The temperature-dependent characteristics of MDLs were studied as well. The substrate temperature was varied from 288 to 323 K without any additional heat sinks. Figure 3(c) plots L-L curves at different temperatures. The inset plots the natural logarithm of threshold power as a function of temperature. The characteristic temperature (T_0) can be extracted to be 65.8 K by $P_{\rm th}(T_2) = P_{\rm th}(T_1)\exp(T_2 - T_1)/T_0$. This value is much higher compared with other reported T_0 for optically pumped QD MDLs grown on both Si and III-V native substrates [17,24,29].

In addition to MDLs with a membrane thickness of 435 nm discussed earlier, we also fabricated MDLs with a membrane thickness of 280 and 380 nm for further investigation. The ratio between the thickness of the InAlAs cladding layer and InAlGaAs barrier layer was kept identical for different samples.

We first studied the influence of the disk diameter on the lasing wavelength of the MDLs and then moved on to investigate the influence of the membrane thickness. The non-uniform silica beads in colloidal lithography produces MDLs with a small variation of the diameters. After checking the dimension of MDLs by a SEM, the experimental data of MDLs with different membrane thicknesses are summarized in Figs. 4(a)–4(c). The clear trends of the lasing wavelength against the diameter can be seen in all three sets of data. With the expansion of the diameter, the lasing wavelength also increases. For example, for MDL lasers with a membrane thickness of 380 nm [see Fig. 4(b)], the lasing peak increases from 1.57 to 1.61 μm, when the disk diameter increases from 3.75 to 3.8 μm. Interesting, the lasing peak also exhibits a linear trend when the disk diameter further increases from 3.8 to 4 μm. For all three kinds of MDLs, the lasing wavelength range from 1.54 to 1.61 μm, spanning both the C band and L band.

To further investigate the relationship between the diameter and the lasing wavelength of MDLs, we simulated the resonance

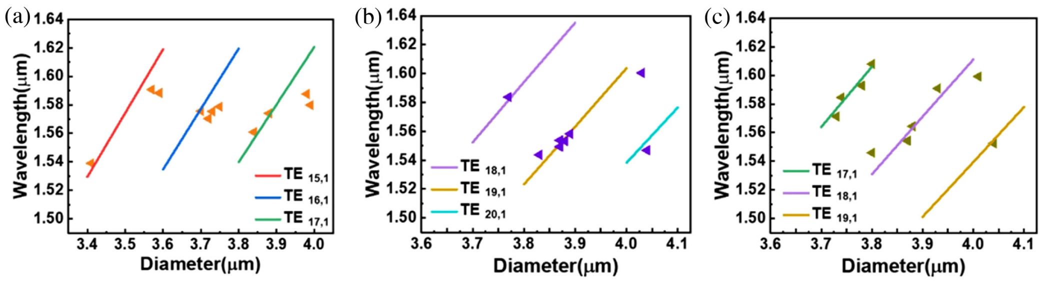

Fig. 4. (a)–(c) Experimental data of MDLs with 275–300, 375–400, and 420–440 nm membranes, respectively. The lines represent the 2D FDTD simulation results based on the representative thicknesses, which are 280, 380, and 435 nm accordingly.

wavelength of MDLs with different structures. In FDTD simulation, some randomly oriented dipole emitters were placed in the microdisk to excite resonance and frequency domain power monitor was used to observe both field spectrum and mode profilers [30,31]. As mentioned above, lasing peak of a single-mode MDL is in good agreement with the simulated TE resonance mode. Therefore, we only include the simulation results of TE modes here. Based on the PL profile of the as-grown sample [Fig. 1(b)], the resonance modes locate between 1.5 and 1.65 μm. The simulation results of MDLs with different membrane thicknesses are also shown in Figs. 4(a)–4(c). For MDLs of each thickness, there are different modes included in different diameter ranges. The simulated wavelength of specific mode increases with the increase of diameter. This relationship can be explained by the equation for the resonance wavelength calculation $\lambda = 2\pi R n_{\mathrm{eff}}/m$, where n_{eff} is the modal effective refractive index, and m is the azimuthal mode number [32]. For a mode with specific m, when the diameter keeps increasing, the peak wavelength will keep increasing and finally move out of the PL profile. Meanwhile, new modes with higher azimuthal mode numbers will be introduced into the PL range and linearly increase with the expansion of disk diameter similarly. The simulation results agree well with the experimental data in all three kinds of MDLs. This reveals the feasibility of wavelength control via the diameter design. By changing the length of the optical path of the microdisk cavity, the diameter could adjust the lasing wavelength λ of the MDL. E-beam lithography could be applied to define the diameter for more precise lasing wavelength control of MDLs.

We note that in experimental data, MDLs with similar diameters can achieve lasing at different modes. For example, for MDLs with a membrane thickness of 380 nm and diameter of 3.8 μm, both $TE_{17,1}$ and $TE_{18,1}$ mode lasing were found [see Fig. 4(b)]. The reason is that two modes are usually included in the PL profile when considering the spectra range of the simulation and the FSR of MDLs [see Fig. 3(a)]. To control the resonance wavelength accurately and consistently in one mode, the influence of the overlapping of different modes could be lessened by enlarging mode spacing. Based on the equation for the FSR calculation, a possible method is to further miniature the diameter of the MDL.

In addition to the disk diameter, the relationship between the microdisk membrane thickness and lasing wavelength is also studied based on the experimental and simulation results. To rule out the influence of modes with different azimuthal mode numbers, we chose the $TE_{17,1}$ mode that was found in MDLs with a membrane thickness of 280 and 380 nm. As

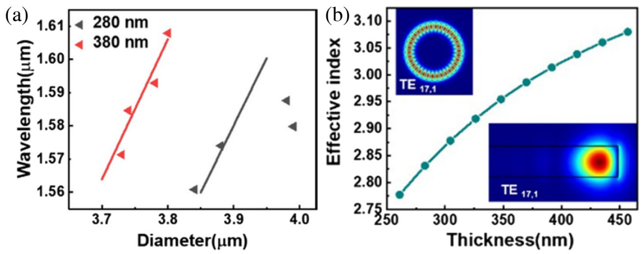

Fig. 5. (a) Experimental data of $TE_{17,1}$ mode lasing MDLs with 275–300 and 375–400 nm membranes. The lines represent the FDTD simulation results. (b) Effective index of a microdisk membrane against the thickness of the membrane, where the ratio of thickness of the InAlAs cladding layer and InAlGaAs spacer layer is kept the same. Inset: mode profile and cross-sectional slice of the simulated $TE_{17,1}$ mode.

shown in Fig. 5(a), for a similar wavelength, we observed a much smaller diameter of MDL with a 380 nm thick membrane when comparing with 280 nm thick membranes. It can be attributed to different effective indices of microdisk membranes of different thicknesses [33,34]. Therefore, we theoretically calculated the effective index of a microdisk membrane using a FDTD method. Figure 5(b) presents the simulation results. The effective index of the microdisk membrane increases with the increase of membrane thickness. According to the resonance wavelength equation $\lambda = 2\pi R n_{\mathrm{eff}}/m$, when the effective index becomes larger, the wavelength will get increased. These results can clearly explain the different diameter ranges of the identical mode in MDLs with different membrane thicknesses. This also suggests that we can control the wavelength of MDLs by the design of the membrane thickness.

The thickness-effective index curve also helps to explain the deviation of the experimental data from the simulation results. Although the effective index increases with the increase of membrane thickness, the slope gradually decreases, which means that influence induced by thickness increase keeps getting weaker. In all three fabricated samples, there were some slight variations of the membrane thickness, and we only chose the representative thickness for simulation. We observed some large deviations between the experimental data and simulation results in 280 nm thick MDLs [see Fig. 4(a)], because even small variations in thickness would induce a substantial change of the effective index. In parallel, the slope difference can also be proved in another two sets of data with thicker membranes. Shown in Figs. 4(b), the experimental data of 380 nm thick MDLs are in good agreement with the simulated $TE_{17,1}$ and $TE_{18,1}$ modes. This reflects a small influence of thickness variation on wavelength. As a result, a microdisk membrane with a suitable thickness will help to reduce the possible impact induced by thickness variation on wavelength control.

The analysis of the experimental data and simulation results show the feasibility of wavelength control based on the membrane thickness and diameter of our QDash MDL. Based on the results, we suggest a means to manipulate the lasing wavelength, making the MDL a superior light source candidate of for specific wavelength operation. Besides, we can realize the multi-channel communication easily by fabricating MDLs with different diameters on a single sample. Compared with other multi-wavelength arrays demonstrated in literatures [35,36], both the volume of light sources and the fabrication complexity can be reduced. In the future, the diameter of MDLs can be further minimized to a sub-wavelength scale for continuous wavelength controlling within an FSR. QDash MDLs provide a notable advantage in scaling to small dimensions through reduced sidewall recombination. Therefore, investigation on electrically driven WGM laser could be carried out as well. The small volume compared to the larger FP geometries would help to provide a lower lasing threshold and denser integration. Additionally, assisted with FDTD simulation, designs such as gratings could help to achieve lasers with more reliable lasing performance for further optoelectronics integration.

In summary, we demonstrated, to the best of our knowledge, the first 1.55 μm RT CW InP-based InAs QDash MDL laser directly grown on (001) Si. The average threshold is 200 and 500 μW for MDLs on InP and Si substrates, respectively. The highest operation temperature of 323 K was achieved at MDLs on Si. We also studied and proved that the lasing wavelength of MDLs could be well controlled by the disk diameters and the membrane thickness. The lasing wavelengths cover both the C band and L band, suggesting a wide range for the wavelength design. Our results show the capability of MDLs as light sources in dense optoelectronics integration and provide a simple way to achieve multi-wavelength operations for on-chip communication.

Funding. Research Grants Council, University Grants Committee (16212115, 16245216); Innovation and Technology Fund (ITS/273/16FP).

Acknowledgment. The authors would like to thank staff at the Nanosystem Fabrication Facility and Materials Characterization and Preparation Facility of the Hong Kong University of Science and Technology for technical support. Helpful discussions with Y. Han are also acknowledged.

Disclosures. The authors declare no conflicts of interest.

Data Availability. Data underlying the results presented in this paper are not publicly available at this time but may be obtained from the authors upon reasonable request.

REFERENCES

1. D. Thomson, A. Zilkie, J. E. Bowers, K. Tin, G. T. Reed, L. Vivien, D. M. Morini, E. Cassan, L. Virot, J. M. Fédéli, J. M. Hartmann, J. H. Schmid, D. X. Xu, F. Boeuf, P. O'Brien, G. Z. Mashanovich, and M. Nedeljkovic, J. Opt. **18**, 073003 (2016).
2. A. H. Atabaki, S. Moazeni, F. Pavanello, H. Gevorgyan, J. Notaros, L. Alloatti, M. T. Wade, C. Sun, S. A. Kruger, H. Meng, K. A. Qubaisi, I. Wang, B. Zhang, A. Khilo, C. V. Baiocco, M. A. Popović, V. M. Stojanović, and R. J. Ram, Nature **556**, 349 (2018).
3. X. Wang and J. Liu, J. Semicond. **39**, 061001 (2018).
4. Z. Zhou, B. Yin, and J. Michel, Light Sci. Appl. **4**, e358 (2015).
5. Y. Wan, Z. Zhang, R. Chao, J. Norman, D. Jung, C. Shang, Q. Li, M. J. Kennedy, D. Liang, C. Zhang, J. W. Shi, A. C. Gossard, K. M. Lau, and J. E. Bowers, Opt. Express **25**, 27715 (2017).
6. Y. Han and K. M. Lau, J. Appl. Phys. **128**, 200901 (2020).
7. Y. Han, Y. Xue, Z. Yan, and K. M. Lau, J. Lightwave Technol. **39**, 940 (2021).
8. T. Zhou, M. Tang, G. Xiang, B. Xiang, S. Hark, M. Martin, T. Baron, S. Pan, J. S. Park, Z. Liu, S. Chen, Z. Y. Zhang, and H. Y. Liu, Nat. Commun. **11**, 977 (2020).
9. R. Beanland, A. M. Sanchez, D. Childs, K. M. Groom, H. Y. Liu, D. J. Mowbray, and M. Hopkinson, J. Appl. Phys. **103**, 014913 (2008).
10. A. Y. Liu, S. Srinivasan, J. Norman, A. C. Gossard, and J. E. Bowers, Photonics Res. **3**, B1 (2015).
11. J. Kwoen, B. Jang, J. Lee, T. Kageyama, K. Watanabe, and Y. Arakawa, Opt. Express **26**, 11568 (2018).
12. J. C. Norman, D. Jung, Y. Wan, and J. E. Bowers, APL Photonics **3**, 030901 (2018).
13. M. Liao, S. Chen, Z. Liu, Y. Wang, L. Ponnampalam, Z. Zhou, J. Wu, M. Tang, S. Shutts, Z. Liu, P. M. Smowton, S. Y. Yu, A. Seeds, and H. Y. Liu, Photonics Res. **6**, 1062 (2018).
14. Y. Xue, W. Luo, S. Zhu, L. Lin, B. Shi, and K. M. Lau, Opt. Express **28**, 18172 (2020).
15. S. L. McCall, A. F. J. Levi, R. E. Slusher, S. J. Pearton, and R. A. Logan, Appl. Phys. Lett. **60**, 289 (1992).
16. Y. Wan, Q. Li, A. Y. Liu, A. C. Gossard, J. E. Bowers, E. L. Hu, and K. M. Lau, Opt. Lett. **41**, 1664 (2016).
17. S. Zhu, B. Shi, Y. Wan, E. L. Hu, and K. M. Lau, Opt. Lett. **42**, 679 (2017).
18. B. Shi, S. Zhu, Q. Li, Y. Wan, E. L. Hu, and K. M. Lau, ACS Photonics **4**, 204 (2017).
19. S. Zhu, B. Shi, Q. Li, Y. Wan, and K. M. Lau, Opt. Express **25**, 31281 (2017).
20. W. Q. Wei, J. Y. Zhang, J. H. Wang, H. Cong, J. J. Guo, Z. H. Wang, H. X. Xu, T. Wang, and J. J. Zhang, Opt. Lett. **45**, 2042 (2020).
21. W. Luo, Y. Xue, J. Huang, L. Lin, B. Shi, and K. M. Lau, Photonics Res. **8**, 1888 (2020).
22. Y. Wan, Q. Li, A. Y. Liu, A. C. Gossard, J. E. Bowers, E. L. Hu, and K. M. Lau, Appl. Phys. Lett. **109**, 011104 (2016).
23. Y. Wan, J. Norman, and J. E. Bowers, in *Future Directions in Silicon Photonics*, S. Lourdudoss, J. E. Bowers, and C. Jagadish, eds. (Academic, 2019), p. 305.
24. T. Ide, T. Baba, J. Tatebayashi, S. Iwamoto, T. Nakaoka, and Y. Arakawa, Opt. Express **13**, 1615 (2005).
25. Y. Chu, A. Mintairov, Y. He, J. Merz, N. Kalugnyy, V. Lantratov, and S. Mintairov, Phys. Status Solidi C **8**, 325 (2011).
26. M. J. Mondry, D. I. Babic, J. E. Bowers, and L. A. Coldren, IEEE Photonics Technol. Lett. **4**, 627 (1992).
27. D. S. Song, J. K. Hwang, C. K. Kim, I. Y. Han, D. H. Jang, and Y. H. Lee, IEEE Photonics Technol. Lett. **12**, 954 (2000).
28. C. Seassal, X. Letartre, J. Brault, M. Gendry, P. Pottier, P. Viktorovitch, O. Piquet, P. Blondy, D. Cros, and O. Marty, J. Appl. Phys. **88**, 6170 (2000).
29. T. Yang, A. Mock, J. D. O'Brien, S. Lipson, and D. G. Deppe, Opt. Express **15**, 7281 (2007).
30. A. C. Tamboli, E. D. Haberer, R. Sharma, K. H. Lee, S. Nakamura, and E. L. Hu, Nat. Photonics **1**, 61 (2007).
31. S. Sant, A. Schenk, B. Mayer, S. Wirths, S. Mauthe, H. Schmid, and K. E. Moselund, in *International Conference on Numerical Simulation of Optoelectronic Devices (NUSOD)* (2018), p. 79.
32. W. Noh, M. Dupré, A. Ndao, A. Kodigala, and B. Kanté, ACS Photonics **6**, 389 (2019).
33. M. K. Chin, D. Y. Chu, and S. T. Ho, J. Appl. Phys. **75**, 3302 (1994).
34. R. P. Wang and M. M. Dumitrescu, J. Appl. Phys. **81**, 3391 (1997).
35. J. Zhao, X. Chen, N. Zhou, X. Huang, M. Cao, L. Wang, and W. Liu, Opt. Commun. **339**, 78 (2015).
36. X. Liang, X. Zhang, Y. Y. Chen, and Y. S. Zhang, Optik **202**, 163557 (2020).